Scalable and controlled creation of nanoholes in graphene by microwave-assisted chemical etching for improved electrochemical properties

Dini Wang[†], Rui Dai[‡], Xing Zhang[‖], Yongfeng Lu[⁑], Yan Wang[‖], Yiliang Liao[‖], Qiong Nian[†‡*]

[†]Department of Material Science and Engineering, [‡]Department of Mechanical Engineering,
School of Engineering for Matter, Transport and Energy, Arizona State University, Tempe, AZ
85287, USA

[‖]Department of Mechanical Engineering, University of Nevada, Reno, NV 89557, USA

[⁑]Department of Electrical & Computer Engineering, University of Nebraska-Lincoln, Lincoln,
NE 68588, USA

*Corresponding author. Email: qiong.nian@asu.edu

ABSTRACT: Nanoscale defects, such as nanoholes and edge sites, on the basal plane of two-dimensional (2D) material can provide abundant mass transport channels and chemically active sites for enhancing the electrochemical performance. In this respect, extensive research has been carried out on thermal chemical etching in recent years for manufacturing 2D materials with these defects. However, existing studies found the conventional bulk heating process lacks capability to promote the etching reactions and thus results in the insufficient process efficiency, scalability, and controllability. To address this issue, we report a novel process utilizing microwave irradiation to promote and control the chemical etching of 2D materials. In this process, the microwave can induce a selective heating of 2D materials in the liquid solution and then facilitate the etching reactions occurring on the material-etchant interface. Applying this strategy to manufacturing graphene with nanoholes, namely holey graphene, a remarkable reduction of processing time from hour-scale to minute-scale compared to the conventional approaches have been achieved with the control of the population and area percentage of nanoholes on the basal plane. The obtained holey graphene oxide sheets exhibit excellent capacitive performance and electrochemical catalytic activity due to the improvements in the accessible surface area, ion diffusion, and heterogeneous charge transfer. This study paves a way for large-scale manufacturing of 2D materials with nanoscale defects on the basal plane for a wide range of applications.

KEYWORDS: holey graphene; microwave-assisted synthesis; porous nanostructures; electrochemical energy storage; mass transport; charge transfer.

INTRODUCTION

As one of the most important two dimensional (2D) materials, graphene has attracted enormous attention for being utilized as the active component or conductive additive in electrochemical electrodes of batteries, supercapacitors, catalysts, and sensors, due to its superior electrochemical activity, high electrical conductivity, and large specific surface area.[1-3] Nevertheless, an inevitable limitation of graphene-based electrodes on mass transport is that ions or molecules cannot directly travel across the basal plane of a graphene sheet. Hence, the mass traveling paths in graphene sheets are tortuous and lengthened.[4-5] This reduces the accessible surface area for absorbing substances, such as electrolytes or reactants, leading to the sluggish diffusion kinetics and hindering the performance improvement brought by graphene.[5-6] This issue can be even worse if the graphene sheets are densely assembled with high mass loadings (e.g. >10 mg/cm^2), or start self-wrapping and re-stacking.[6-7] A potential solution to this issue has been proposed of creating nanoholes on the basal planes of graphene sheets. These nanoholes serve as the mass transport channels that allow ions or molecules to directly transport so that the electrolyte accessible surface area of graphene sheets are restored.[4-5] Moreover, the hole-making process would introduce extended edge sites to the graphene basal plane around where the nanoholes are created. These edge-site carbon atoms are more chemically active than the in-plane ones[8-9] and therefore can improve the electrochemical activity of graphene electrodes, making holey graphene very attractive in various electrochemical applications.[10-17] For instance, Xu et al.[5] reported a holey graphene electrode with an ultrahigh gravimetric capacitance of 310 F/g, about 1.5 times higher than that of the pristine graphene. Sun et al.[10] found that by incorporating holey graphene with transition metal oxides, the nanocomposite can realize the outstanding rate capability and specific capacity with a mass loading high enough for practical applications.

Despite the highly promising electrochemical characteristics of holey graphene, the manufacture of this material is challenging due to the structural inertness of graphene lattice and the high covalent bond strength among the sp^2-hybridized carbon atoms. For these reasons, holey graphene is generally fabricated from graphene oxide (GO) that has weaker sp^3 bonds in the lattice,[18] which can be chemically etched to form through-the-thickness nanoholes. Various fabrication methods have been reported, including steam etching,[19] refluxing or sonicating with nitric acid,[12, 20] chemical activation,[21] catalytic oxidation,[22-23] photocatalytic oxidation,[24] etc. However, these methods designed for specific applications often suffer from issues such as chemical contamination or deterioration to the graphene structure. To tackle this challenge, Duan et al.,[5, 25] recently developed an approach to fabricating holey graphene by heating GO solution with hydrogen peroxide etchant followed by reduction process, through which they obtained products with both high specific surface area (1560 m^2/g)[5] and electrical conductivity (2030 S/m)[25]. This simple and green method has been prevalent for holey graphene fabrication since then.[15-17, 26-28] However, it is still time- and energy-consuming, since a constant bulk heating for several hours at around 100 °C is required to obtain products, and a considerable amount of energy can be dissipated to the ambient environment. The low process efficiency is attributed to the fact that bulk heating process lacks the capability to promote graphene-etchant reactions in their interface. Besides, the long-period treatment under the boiling temperature can lead to the decomposition of hydrogen peroxide molecules before they react with GO sheets.

Alternative methods for holey graphene fabrication have been proposed, such as heating and oxidizing in air[13-14, 29-31] or direct exfoliation from graphite[32-33]. Despite their potential in fabrication scalability, these solid-phase methods have an inherent issue on dispersing graphene materials and etchants to ensure the homogeneity of chemical reactions. The inhomogeneous reactions consequently lead to the non-uniform formation of nanoholes and bring difficulty in quality control. On the contrary, the liquid-phase methods mentioned above are not only favorable to obtain holey graphene with more uniform properties but also superior in process continuity.

This is because that the fabrication of GO, which is the starting material for holey graphene fabrication (except for the direct exfoliation method[32-33]), is dominated by the liquid-phase route that has been offering low-cost graphene products for a broad range of applications during over a decade's growth of the graphene industry.[34] In this respect, a fast, scalable, controllable, cost-effective, and solution-based fabrication method of holey graphene is still highly desirable. In addition, the mechanism of nanoholes nucleation and growth also deserves a systematical study for controlling the population and size of the holes on the graphene basal plane.

Herein, this paper reports a novel method for holey graphene fabrication via microwave-assisted chemical etching (MACE) of the GO solution. This process couples vigorous chemical attack with rapid electromagnetic wave irradiation to reduce the processing time from hour-scale to minute-scale. The mechanism of MACE process is revealed through a comparison study emphasizing on the in situ heat generation and selective heating of GO sheets in the solution under microwave irradiation. Moreover, a simple two-step strategy is developed to effectively control the population and area percentage of the nanoholes on the holey graphene sheets. By using transmission electron microscopy (TEM), X-ray photoelectron spectroscopy (XPS), and Raman spectroscopy, the microstructural evolutions, including the changes in the atomic ratio, defect density, and the number of functional groups, are analyzed to understand the formation and growth mechanisms of nanoholes during each step of fabrication. The capacitive performance and electrochemical catalytic activity of the holey graphene sheets are evaluated. By adjusting the microstructure of nanoholes via the two-step strategy, we further demonstrate the versatile potentials of this material with tunable electrochemical properties.

RESULTS AND DISCUSSION

Holey Graphene Fabrication.

The schematic diagram of the two-step MACE method for holey graphene fabrication is illustrated in Figure 1a. First, the bare GO aqueous solution is pretreated under microwave irradiation for 90–360 s using a microwave reactor (Figure S1) without any etchant, aiming to mildly reduce GO before etching. In the reduction of GO, when the oxygen-containing functional groups are removed from the graphene lattice, the surrounding carbon atoms can be taken away at the same time forming CO or CO_2 and leaving behind vacancies on the lattice.[35] Thus, the first-step processing can create single/few-atom vacancy defects on GO sheets. Then, in the second step, the defected GO (dGO) solution is mixed with hydrogen peroxide and irradiated again in the microwave reactor for 45–180 s. Assisted by the microwave irradiation, the hydrogen peroxide molecules react with GO and remove carbon atoms from the lattice, especially the carbon atoms around vacancy defects since they are more chemically active.[9, 36-37] The atom removal leads to the formation of nanoholes on the graphene basal plane. The ultra-high process efficiency is ascribed to the unique selective heating by microwave irradiation on the GO-etchant interface, which will be explained in the following sections. Eventually, a certain amount of holey GO (hGO) solution is obtained depending on the volume of the microwave reactor.

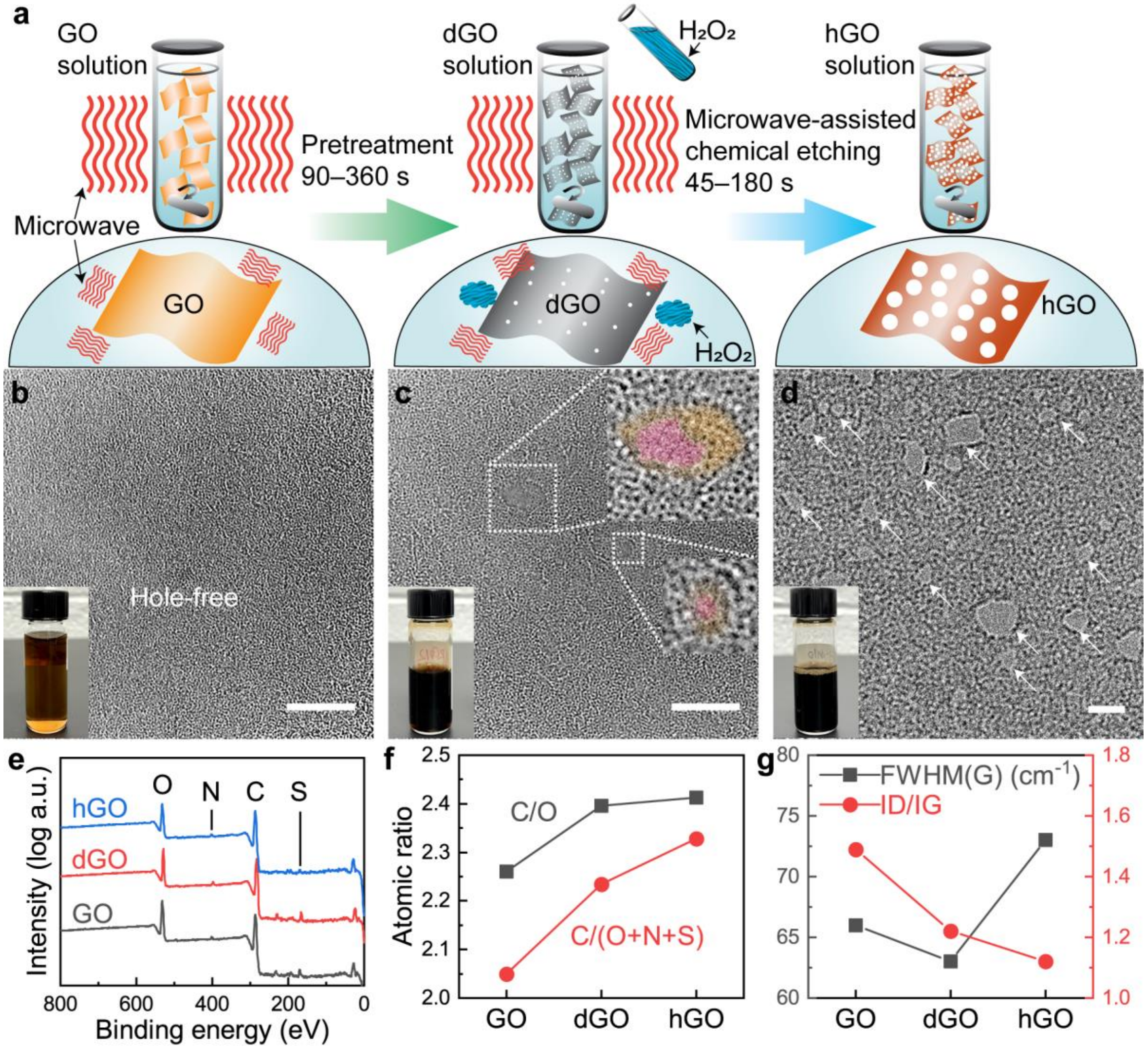

Figure 1. Holey graphene fabrication via MACE with a two-step strategy. (a) Schematic of the fabrication process; TEM images of (b) pristine graphene oxide (GO), (c) defected graphene oxide (dGO), and (d) holey graphene oxide (hGO); (e) XPS spectra; (f) C/O and C/(O+N+S) atomic ratios obtained from XPS spectra; (g) full width at half-maximum of the G band (FWHM(G)) and intensity ratios of the D to G band (I_D/I_G) obtained from Raman spectra. Insets in the bottom-left corners of b–d are the digital images of the aqueous solutions. Insets in c magnify the locations of nanoholes and highlight the holes (red) and functional-group-depleted regions (yellow). Scale bars in b,c, 5 nm; in d, 20 nm.

The morphology evolution of the pristine GO, dGO, and hGO sheets at different stages of fabrication were characterized by TEM, as shown in Figures 1b–d. The pristine GO sheet (Figure 1b) does not show any recognizable holey region on the basal plane, and the color of its aqueous solution is light brown (the inset in Figure 1b). Within an area of the same size on the dGO sheet (Figure 1c), two nanoholes with diameters of about 0.5 and 3.0 nm (the insets in Figure 1c) are found, and the color of the dGO solution turns darker (the inset in Figure 1c), suggesting the reduction of GO during the pretreatment.[38-39] The yellow regions in the insets of Figure 1c show that the functional groups are depleted in the areas around the nanoholes, while other areas on the dGO sheet are still covered by functional groups. This clearly suggests that the formation of the nanoholes on the dGO sheets are strongly related to the removal of functional groups. However, the sole reduction process (i.e. the removal of functional groups) cannot bring the formation of abundant nanoholes, and an etching reagent such as hydrogen peroxide is necessary. As shown in Figure 1d, with the coupling effect of microwave irradiation and chemical etching, the nanoholes with a high density and diameters up to about 25 nm are observed on the basal plane of the hGO sheet. According to the AFM images (Figure S2), no obvious change is identified from GO to hGO in both thickness (about 1 nm) and size (μm-scale), implying that both the microwave exposure and etchant concentration are in the appropriate ranges to avoid disintegrating the GO sheets into small pieces.

The XPS spectra of the pristine GO, dGO, and hGO sheets (Figure 1e) show that they are mainly composed of C, O, S, and N atoms. By calculating the C/O or C/(O+N+S) atomic ratio from the XPS spectra, we can analyze the constituent change during each fabrication step. As indicated by the higher C/O ratio of dGO relative to GO (Figure 1f), the microwave irradiation during the pretreatment causes a partial removal of the oxygen-containing functional groups from GO sheets.

If the sulfur- and nitrogen-containing groups are considered, the pretreatment still brings an increase in terms of C/(O+N+S) from 2.05 to 2.23. After the MACE, the hGO sheets show a negligible increase of the C/O ratio from 2.40 to 2.41, suggesting that the losses of carbon and oxygen atoms were balanced during this step. The oxygen supply of hydrogen peroxide led to the formation of new oxygen-containing groups on GO sheets, equalizing the removal of oxygen-containing groups caused by the microwave irradiation. This is an obvious distinction between the MACE and conventional chemical-etching methods, which generally show a lower C/O ratio after etching.[5, 10, 17, 27] The increase of the C/(O+N+S) ratio from 2.23 to 2.33 after the MACE indicates that the removal of sulfur- and nitrogen-containing groups on GO sheets are significant in this step.

Raman spectroscopy was employed to characterize the disorder level of GO sheets, i.e. the distortion of sp^2 graphitic rings on the graphene lattice affected by both defects and functional groups.[40] Research has reported that the disorder level of GO grows with the full width at half-maximum (FWHM) of the G band, one of the characteristic peaks in the Raman spectra of graphitic structures.[41-42] The FWHM(G) of GO (Figure 1g) decreases from 66 to 63 cm^{-1} after the pretreatment and increases to 73 cm^{-1} after the MACE, suggesting that the graphitic arrangements of the graphene lattice is first restored by the pretreatment and then distorted by the MACE. Although the pretreatment creates the vacancy defects that distort the graphene lattice, the disorder level of dGO is actually affected more by the removal of functional groups during the pretreatment. The MACE, on the other hand, significantly promotes the disorder level by forming the nanoholes that cause large lattice distortion on hGO sheets. In addition, the intensity ratio of the D to G band (I_D/I_G) is another commonly used indicator of the disorder level on GO sheets. Cançado et al.[43] report that with the increase of FWHM(G), the I_D/I_G ratio of the single-layer graphene first grows within a low-disorder range and then reduces when entering the high-disorder range. In this study, the correlations between FWHM(G) and I_D/I_G (Figure S3a) of all the GO, dGO, and hGO samples exhibit the similar trends. The values of FWHM(G) and I_D/I_G become lower from GO to dGO, while the hGO samples show mostly higher FWHM(G) and lower I_D/I_G than GO. It confirms that the dGO samples are in the low-disorder range where I_D/I_G increases with the disorder level, while the hGO samples are in the high-disorder range where I_D/I_G reduces with the disorder level. Also, it is found that FWHM(D) is a similar indicator as I_D/I_G to determine the disorder level of GO (Figures S3b and S3c).

Controllable Formation and Growth of Nanoholes.

Differed from most solution-based methods of holey graphene fabrication,[15-17, 26-28] our two-step approach can control the formation and growth of nanoholes by tuning the processing parameters of the pretreatment and MACE. This enables microstructural engineering of holey graphene to meet requirements of various applications. To understand the effect of pretreatment on microstructural features of nanoholes, a group of dGO samples were prepared with pretreatment duration of 90 (denoted as dGO-PS), 180 (denoted as dGO-PM), and 360 s (denoted as dGO-PL), respectively. After the MACE with the same condition (at 50 W for 90 s), the samples were denoted as hGO-PS, -PM, and -PL, respectively. Figures 2a–c present the TEM images of the hGO sheets. The statistics data of the nanoholes in these TEM images, including the total area percentage (%), population (/μm^2), range of diameter (nm), median diameter (nm), and average diameter (nm), are collected (see values in Table S1) and compared in the radar chart (Figure 2d).

With the shortest pretreatment, the TEM image of hGO-PS (Figure 2a) displays a few sparsely scattered nanoholes with the range of diameter widely spread from 7 to 22 nm (Figure S4a). The nanoholes of hGO-PS exhibit the lowest population (45 μm^{-2}) and area percentage (0.6%) because the 90-s pretreatment only creates a limited number of vacancy defects as the formation sites of nanoholes. The low defect density on the dGO-PS sheets is related to the low reduction level of dGO-PS indicated by the Raman and XPS results of dGO-PS (Figures S2a and S5a): the C/O and C/(O+N+S) ratios of dGO-PS are the lowest among all the dGO-P samples; the decrease in I_D/I_G from GO (1.49) to dGO-PS (1.33) is also the smallest. As a result, the formation of nanoholes on the hGO-PS sheets is not prominent after the MACE. This can be also confirmed by the negligible increase in FWHM(G) from 64 cm^{-1} to 66 cm^{-1} (Figure 2e). Nevertheless, the nanoholes of hGO-PS have the largest average and median diameters (13.4 and 11 nm). During the MACE, the limited population of defect regions on the dGO-PS sheets causes the constant etching of a few preferential locations on the lattice where more carbon atoms are removed compared to the other samples.

With longer pretreatment, the nanohole population of hGO-PM drastically grows to 1687 μm^{-2}, bringing the high area percentage (2.1%) that generates the highest disorder level among all the samples (indicated by the largest FWHM(G) of 73 cm^{-1}, Figure 2e). The nanoholes of hGO-PM exhibit the smallest values in the range of diameter (2.5–13.0 nm), average and median diameters (4.0 and 3.5 nm). As indicated by the lower FWHM(G) of dGO-PM relative to dGO-PS (Figure 2e), the longer pretreatment causes a higher reduction level of dGO-PM, meaning the formation of more vacancy defects on the dGO-PM sheets. During the MACE, the dGO-PM sheets can provide many chemically active sites for the etching reaction, resulting in a uniform formation of abundant nanoholes on the hGO-PM sheets.

As the pretreatment duration increases to 360 s, the total area percentage of nanoholes of hGO-PL surges significantly to 6.0% with a large average diameter of 7.2 nm. As indicated by the largest C/O and C/(O+N+S) ratios (Figure S5a) among all the dGO-P samples, the highest reduction level of dGO-PL leads to large numbers of defects created during the pretreatment, promoting the nanohole formation on the hGO-PL sheets. Many nanoholes joined each other during the MACE, forming much larger nanoholes with the diameters up to 53 nm (Figure 2c). The joining of nanoholes leads to a slight drop in population and a broader range of diameter on hGO-PL relative to hGO-PM. However, the diameters of most nanoholes are still smaller than 5 nm (Figure S4c). In fact, if we assume the average diameter of nanoholes is constant under a same processing condition during the MACE, a theoretical nanohole population (that has eliminated the effect of joining) of hGO-PL can be estimated using the average diameter of nanoholes of hGO-PM (4.0 nm) and the area percentage of hGO-PL (6.0%). The calculated value is 4775 μm^{-2}, much larger compared to hGO-PM (1687 μm^{-2}). It leads us to further consider the possibility of limiting the joining of nanoholes by varying the duration of MACE.

Figure 2f illustrates the effect of pretreatment duration on the microstructure of nanoholes. With longer pretreatment, more functional groups can be removed from GO sheets, and a higher density of vacancy defects can be generated. During the MACE, these vacancy defects are constantly enlarged into nanoholes. Therefore, more nanoholes can be obtained on the hGO sheet with longer pretreatment. However, if the pretreatment is too long, the crowded nanoholes would join each other during the MACE, leading to the decrease of population. To effective tune the population of nanoholes, the MACE duration should be adjusted accordingly to control the growth of nanoholes.

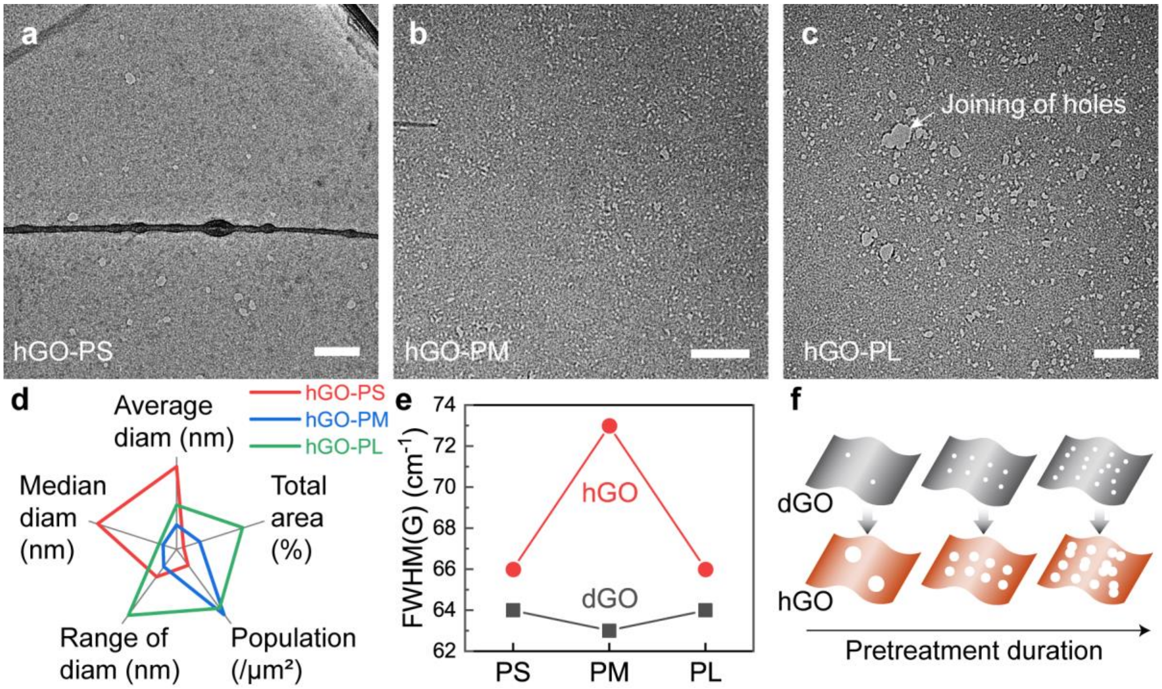

Figure 2. Holey graphene oxide (hGO) sheets prepared with different pretreatment duration. TEM images of hGO pretreated for (a) 90, (b) 180, and (c) 360 s; (d) radar chart comparing the total area percentage, population, range of diameter, median diameter, and average diameter of the nanoholes in a–c; (e) FWHM(G) obtained from the Raman spectra of defected graphene oxide (dGO) and hGO; (f) schematic showing the effect of pretreatment on the microstructure of hGO. Scale bars in a–c, 100 nm.

To study the effect of MACE Another group of hGO sheets were prepared on the growth of nanoholes. The GO solutions were first pretreated under microwave for 180 s (the same as dGO-PM) to obtain a decent defect density on dGO as demonstrated above. Then, the dGO samples were etched for 45 s (denoted as hGO-ES), 90 s (denoted as hGO-EM), and 180 s (denoted as hGO-EM), respectively. TEM images of the hGO-E samples are shown in Figures 3a–c, and the statistics data of the nanoholes are collected (Figure S6) compared in the radar chart (Figure 3d).

After the MACE of 45 s, small nanoholes (5.6 nm) are observed on hGO-ES with a relatively low population (454 μm^{-2}), while the range of diameter is narrow (3.5–18 nm). The emerging of nanoholes from vacancy defects is more obvious than the size growth of nanoholes. This is because that the short duration of MACE limits the etching of GO sheets. Both the C/O ratio (Figure S4b) and FWHM(G) (Figure 3e) show no obvious change caused by the short duration of MACE.

The longer MACE brings a drastic growth in the population of nanoholes to 1050 μm^{-2}. Compared to hGO-ES, hGO-EM shows a larger total area percentage of nanoholes (3.1%) and higher disorder level with FWHM(G) of 73 cm^{-1} (Figure 3e). The range of nanohole diameter of hGO-PM become broader (3.5–31 nm) because of the joining and preferential growth of nanoholes during the 90-s MACE.

The MACE of 180 s results in a major boost both in the total area percentage (10.7%) and average diameter (10.3 nm) of nanoholes with a high population of 1295 μm^{-2}. The range of diameter further broadens (3.5–65 nm). Many joined holes with diameters over 20 nm are observed on the hGO-EL sheet (Figure 3c). The disorder level of hGO-EL is the highest among all hGO-E samples, as indicated by FWHM(G) (Figure 3e). Both the I_D/I_G and C/O ratios of hGO-EL (Figures S3a and S5b) abnormally increase after the MACE due to a higher reduction of GO induced by the microwave irradiation with long duration.

The mechanism of MACE is illustrated in Figure 3f. In contrast to the effect of pretreatment, which mainly changes the population of nanoholes on hGO, the MACE process affects both the formation and growth of nanoholes by coupling chemical etching and microwave irradiation. With a moderate defect density on the dGO sheets, the longer duration of MACE brings a larger nanohole population but also the joining and preferential growth of nanoholes that increase the range of diameter and total area percentage. Therefore, the short duration of MACE is favorable to form the nanoholes with relatively uniform diameters, while the long duration of MACE contributes most to the high population and total area percentage of nanoholes. By tuning the duration of both pretreatment and MACE, the microstructural features of nanoholes can be effectively controlled.

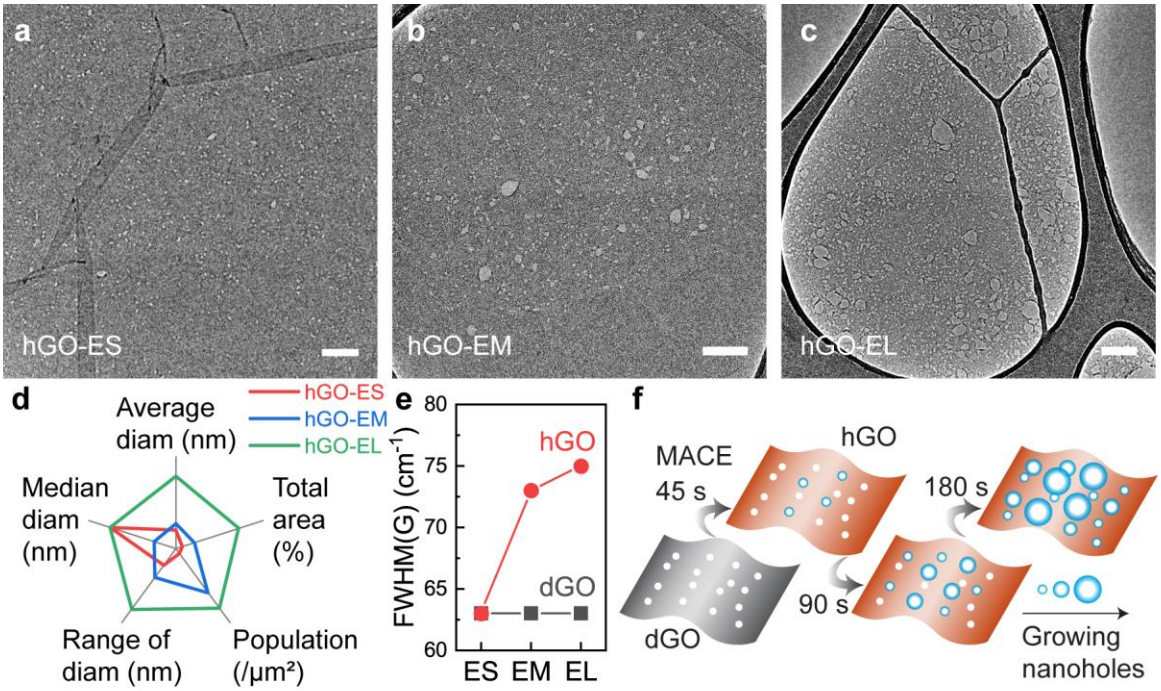

Figure 3. Holey graphene oxide (hGO) prepared with different duration during microwave-assisted chemical etching (MACE). TEM images of hGO etched for (a) 45, (b) 90, and (c) 180 s; (d) radar chart comparing the total area percentage, population, range of diameter, median diameter, and average diameter of the nanoholes in a–c; (e) FWHM(G) obtained from the Raman spectra of defected graphene oxide (dGO) and hGO; (f) schematic of the effect of MACE on the microstructure of hGO. Scale bars in a–c, 100 nm.

Rapid Fabrication Enabled by Selective Heating.

Besides the controllability of the nanohole features, our method provides a promising solution to scalable manufacturing of holey graphene by reducing the total processing time from hour-scale to minute-scale. The rapid process is attributed to the in situ heat generation of GO sheets under microwave irradiation. To understand the heating mechanism of this method, we recorded the temperature and pressure profiles of the de-ionized water, 1 mg/mL, and 3 mg/mL dGO aqueous solutions processed with the same volume (3 mL) under the same condition of microwave irradiation (50 W for 120 s). To avoid the effect of etching reaction, no etchant was added in any of these samples. The final temperatures of the de-ionized water, 1 mg/mL, and 3 mg/mL dGO solutions (Figure 4a) are 140 °C, 145 °C, and 151 °C, respectively. Apparently, a higher dGO concentration leads to the greater energy absorption from the electromagnetic wave. The plot of the temperature increase rates (the inset in Figure 4a) suggests the heating can be divided into two stages: in stage I (0–50 s), the temperature increase rates of the three samples show no obvious difference and fluctuate at around 1.8 °C/s; in stage II (50–120 s), the temperature increase rates all drop to around 0.5 °C/s, while the solution with higher dGO concentration can keep a faster increase. The two-stage heating results from the boiling of water that starts at about 50 s when the pressures inside the sealed reaction tubes of the three samples (Figure 4b) grow over 1 bar. After the start of boiling, the energy absorbed by the solution is transformed to generate water vapor, and the temperature rise of the solution turns to depend on the increase of pressure. Therefore, the solution with higher dGO concentration can absorb greater energy and evaporates more water.

Research has shown that the microwave can cause local electron movements in the π–π network on graphene sheets,[44-46] resulting in the localized Joule heating that can generate high-temperature plasma arcs on graphene powders within 1–2 s.[47] This microwave-induced electronic heating is obviously different from the conventional microwave mechanism that generally relies on the dielectric loss of non-metallic polar molecules. In this study, the dGO sheets have the defects and functional groups for polar movements[48] and the regional π–π networks for local electron movements. Both dielectric heating and localized Joule heating could co-exist during microwave irradiation and cause intense heating on the surface of the dGO sheets. As a result, the dGO sheets in the solution can be selectively and efficiently heated by the microwave. Nevertheless, because of the relatively low reduction level of the dGO sheets and the heat loss to the environment, the final temperature differences between the dGO solutions and de-ionized water are within tens of Celsius degrees (Figure 4a). In spite of the small temperature difference, a huge amount of thermal energy should already be transfered from dGO to ambient water solution due to the very large specific heat capacity of water. This fact also implies the localized temperature on the dGO surface should be much higher than the recorded solution temperature, so that only 3 mg/ml dGO serving as hot spots still can induce an apparent temperature increase of the whole solution.

These results can be employed to demonstrate the mechanism involved in the rapid fabrication of holey graphene via MACE. The selective heating of GO sheets by microwave irradiation is the essential advantage of the MACE method over the conventional one. As shown in Figure 4c, the conventional heating strongly depends on heat conduction and convection within the solution. The heating of a GO sheet is achieved by heat conduction of its surrounding molecules. The hydrogen peroxide molecules can be decomposed before they can react with GO. In contrast, during the MACE (Figure 4d), the GO sheets directly interact with microwave irradiation and quickly become the hot spots dispersed in the solution due to in situ heat generation, providing constant energy to facilitate the etching reaction with the surrounding hydrogen peroxide molecules. This implies both the process efficiency and controllability could be modulated by the microwave irradiation during the MACE process.

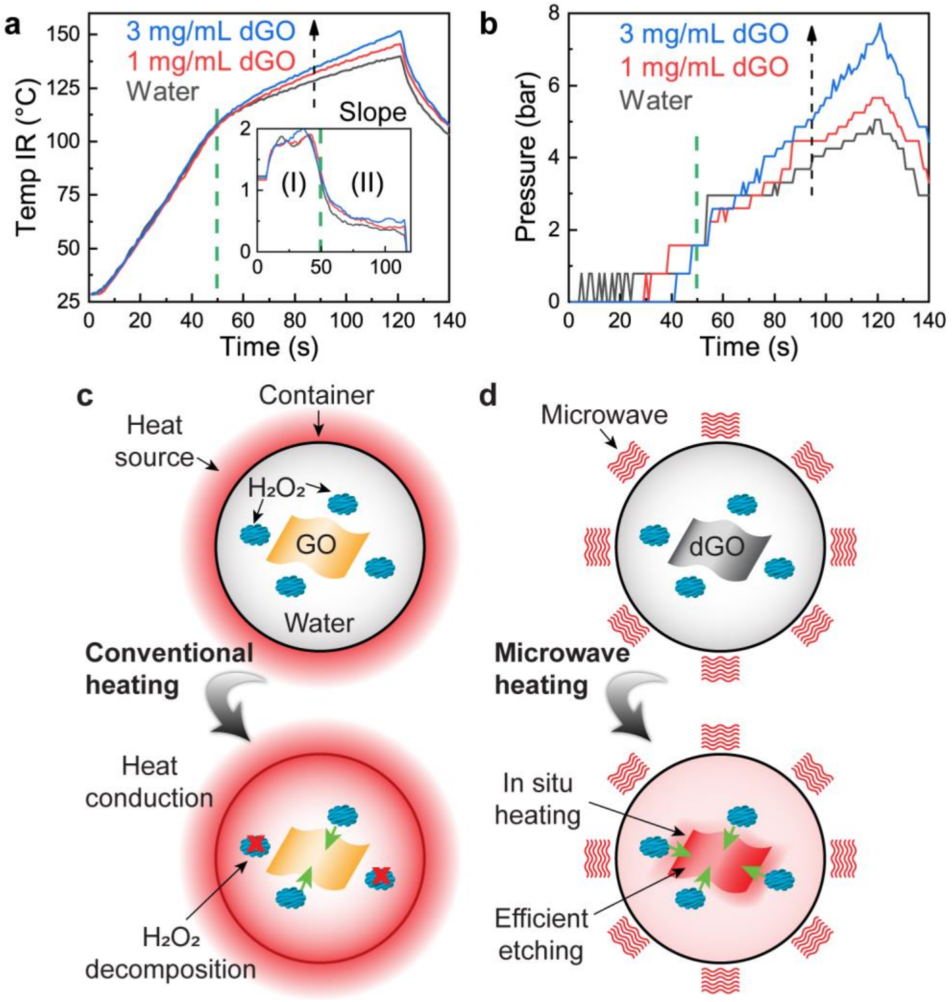

Figure 4. Selective heating of defected graphene oxide (dGO) in aqueous solutions under microwave irradiation. (a) Temperature and (b) pressure profiles of the de-ionized water, 1 mg/mL, and 3 mg/mL dGO solutions processed under the same microwave irradiation; schematics of (c) conventional heating and (d) microwave heating of the GO aqueous solution with the addition of hydrogen peroxide. Inset in a plots the slope of the temperature increase vs. time.

Capacitive performance.

To evaluate the capacitive performance of the holey graphene fabricated via MACE, cyclic voltammetry (CV), electrochemical impedance spectroscopy (EIS), and galvanostatic charge/discharge (GCD) were carried out in the 1 M Na_2SO_4 aqueous electrolyte with a three-electrode cell. Before electrochemical measurements, the hGO sheets were mildly reduced under microwave irradiation to enhance the electric conductivity by restoring π–π network on the lattice.[38, 49] The mildly reduced hGO was denoted as rhGO. For comparison, the rGO electrode was also prepared by reducing GO sheets under the same condition. Figure 5a show the CV curves of the rhGO and rGO electrodes obtained at a scan rate of 50 mV/s. As indicated by the enclosed areas of the CV curves, the specific capacitances of the rhGO electrodes are all higher than that of the rGO electrode (see data in Table 1). The highest specific capacitance of rhGO is 111 F/g, about 3.5 times greater than that of rGO (32 F/g). Note that the capacitance of rGO here is relatively low compared to existing reports,[50] owing to the mild reduction level of GO prepared without any additional agent. Nevertheless, this reduction level is enough to exhibit the significant improvement in capacitive performance brought by the nanoholes. In fact, both the double-layer capacitance and pseudo-capacitance contribute to the capacitive behavior of rhGO and rGO. Compared with rGO, rhGO can provide a larger accessible surface area for double-layer absorption and more electrochemically active sites to promote the pseudo-capacitance. Among the rhGO electrodes fabricated with different duration of pretreatment or MACE, rhGO-PM/EM with a high population and moderate area percentage of nanoholes shows the highest specific capacitance. Although both rhGO-PL and -EL have the population of nanoholes over 1000 /μm^2, their specific capacitances are lower than that of rhGO-PM/EM. The total area percentage of nanoholes on rhGO-PL or -EL is too high to provide a large surface area for double-layer capacitance.

Table 1. Electrochemical properties of reduced holey graphene oxide (rhGO).[a]

Sample	Measurements in sodium sulfate				Measurements in potassium ferricyanide			
	$C_{\mathrm{S,CV}}$	$C_{\mathrm{S,GCD}}$	R_{CT}	D_{W}	ΔE_{P}	R_{CT}	$D_{\mathrm{R\text{-}S}}$	D_{W}
	F/g	F/g	Ω	$\times 10^{-9}$ cm^2/s	mV	Ω	$\times 10^{-6}$ cm^2/s	$\times 10^{-6}$ cm^2/s
rGO	32	25	18	0.17	91	125	2.12×10^{-3}	4.20×10^{-4}
rhGO-PS	48	46	17	1.84	83	107	7.03	8.14
rhGO-PM	111	112	17	3.83	72	98	9.52	8.25
rhGO-PL	91	84	17	2.52	74	96	9.94	8.35
rhGO-ES	44	42	17	1.05	73	104	7.92	7.57
rhGO-EM	111	112	17	3.83	72	98	9.52	8.20
rhGO-EL	77	72	16	2.62	75	99	9.49	9.55

[a] $C_{\mathrm{S,CV}}$ is the specific capacitance calculated from the CV curves measured at 50 mV/s; $C_{\mathrm{S,GCD}}$ is the specific capacitance calculated from the GCD curves measured at 10 A/g; R_{CT} is the charge transfer resistance; D_{W} is the ion diffusion coefficient calculated from the Warburg coefficient; ΔE_{P} is the peak-to-peak separation measured at 10 mV/s; $D_{\mathrm{R\text{-}S}}$ is the ion diffusion coefficient calculated from the Randles-Sevcik equation.

Figure 5b shows the GCD curves of the rhGO and rGO electrodes at a current density of 10 A/g. All curves are close to the triangular shape, and their slopes in the low-voltage range become lower due to the enhancement of pseudo-capacitance. The specific capacitances (Table 1) calculated from the GCD curves agree well with the CV results. At a current density of 0.5 A/g (Figure 5c), the specific capacitance of rhGO-PM/EM is 137 F/g, 4 times of that of rGO (33.8 F/g). When the current density increases to as high as 100 A/g, the rhGO-PM/EM electrode still retains a larger percentage (69%) of the highest specific capacitance relative to rGO (54%), suggesting a better rate capability of rhGO. This should result from the faster transport kinetics of electrolyte ions to the surface of the rhGO sheets.

The EIS measurements were employed to analyze the kinetic process of ion diffusion and charge transfer at the electrode-electrolyte interface. In the Nyquist plot (Figure 5d), the radius of the semicircle in the high-frequency range is proportional to the heterogeneous-charge-transfer resistance (R_{CT}) at the electrode/electrolyte interface, and the slope of the curve in the low-frequency range increase reversely with the Warburg resistance (W) reflecting the ion diffusion process.[51-52] The curves were fitted using the modified Randles circuit[53] (inset in Figure 5d) that includes a resistor for the equivalent series resistance (R_{S}) composed of the solution resistance, contact resistance, and intrinsic resistance of the electrode, a constant phase element due to the limit capacitance (CPE_{L}), a CPE due to the double-layer capacitance (CPE_{DL}), a resistor for R_{CT}, and a Warburg impedance element (W). The R_{S} values in the rhGO and rGO electrodes are within a small range of 2.3–2.4 Ω, because the solution and contact resistances and the reduction level of all samples are the same. The rhGO and rGO electrodes also have similar R_{CT} values of 16–18 Ω (Table 1), while the rhGO electrodes display higher slopes in the low-frequency range (Figures 5d and S8), indicating a faster diffusion-controlled process. To quantify the ion diffusion kinetics in the rhGO and rGO electrodes, we calculated the ion diffusion coefficient via[15, 17, 51]

$$D_{\mathrm{W}} = [RT/(n^2F^2Ac\sigma_{\mathrm{W}})]^2/2 \quad (1)$$

where D_{W} is the ion diffusion coefficient (cm^2/s) calculated using the Warburg coefficient σ_{W} (Ω/s$^{1/2}$), R is the gas constant (J/(K mol)), T is temperature (K), n is the number of electron transfer (here is 1), F is the Faraday constant (C/mol), A is the geometric surface area of the electrode (cm^2), and c is the concentration of Na$^+$ ions (mol/ml). σ_{W} can be further obtained from[51]

$$Z' = (R_{\mathrm{S}} + R_{\mathrm{CT}}) + \sigma_{\mathrm{W}}\omega^{-1/2} \quad (2)$$

where Z' is the real part of the impedance (Ω) and ω is the frequency (s^{-1}). By plotting Z' versus $\omega^{-1/2}$ (i.e. the Warburg plot), σ_{W} can be calculated from the slope of the curve in the low-frequency range. Per eqs 1 and 2, a lower slope in the Warburg plot results in a smaller σ_W and higher D_W. As shown in Figures 5e and S9, all the rhGO electrodes have lower slopes relative to the rGO counterpart. The calculation results (Table 1) show that all the D_W values of rhGO are an order of magnitude higher than that of rGO. Among them, rhGO-PM/EM exhibits the highest value of 3.83×10^{-9} cm^2/s, about 20 times larger than that of rGO (0.17×10^{-9} cm^2/s). It clearly demonstrates that the nanoholes significantly facilitates the ion diffusion kinetics by providing abundant ion transport shortcuts through the rhGO sheets. Among the rhGO electrodes with different duration of pretreatment and MACE, the trend of D_W agrees well with that of specific capacitance calculated from both the CV and GCD curves. The large population and moderate area percentage of nanoholes on rhGO are favorable to improve the accessible surface area and ion diffusion kinetics.

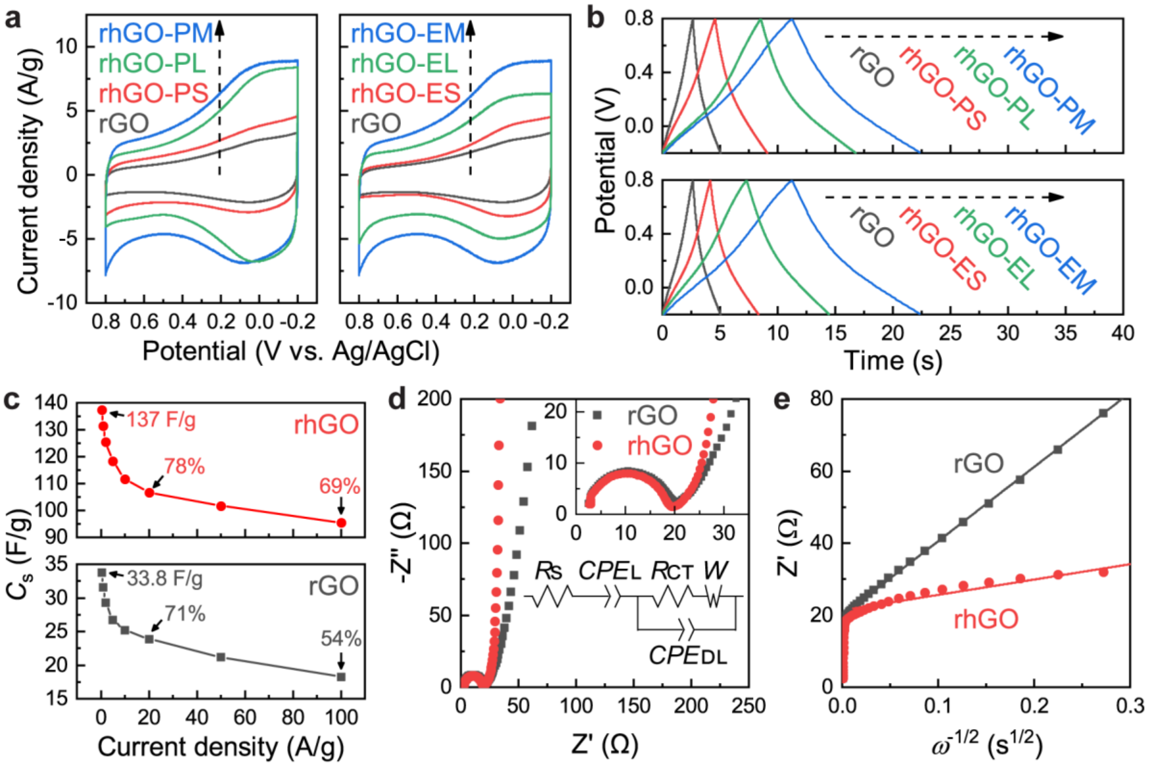

Figure 5. Capacitive performance of reduced holey graphene oxide (rhGO) in 1 M Na_2SO_4. (a) CV curves at a scan rate of 50 mV/s; (b) GCD curves at a current density of 10 A/g; (c) specific

capacitance calculated from the GCD curves vs. current density; (d) Nyquist plot; (e) Warburg plot. Insets in d are the equivalent circuit and the magnified plot in the high-frequency range.

Electrochemical catalytic activity.

To evaluate the electrochemical catalytic activity of rhGO in redox reactions, CV and EIS were measured in the 5 mM $K_3[Fe(CN)_6]$ and 0.1 M KCl aqueous electrolyte. As shown in Figures 6a and 6b, the redox peaks near 0.2 V are observed in all the CV curves of rhGO and rGO. During a negative scan, $[Fe(CN)_6]^{3-}$ ions are reduced to $[Fe(CN)_6]^{4-}$ ions by capturing electrons from the electrode, causing a cathodic current peak; during a positive scan, $[Fe(CN)_6]^{4-}$ ions are oxidized to $[Fe(CN)_6]^{3-}$ ions, generating an anodic current peak.[54] The rhGO electrodes exhibit remarkably higher catalytic activity compared to the rGO counterpart, as indicated by the 40 times higher redox peaks in the CV curves at a scan rate of 10 mV/s. Among the rhGO electrodes (insets in Figures 6a and 6b), the redox peak grows with the area percentage of nanoholes. Higher redox peaks result from both faster redox kinetics and diffusion kinetics. Firstly, more electrochemically active sites around the nanoholes contribute to faster redox kinetics by providing a larger electronic density of states of the electrode material.[55] It can be confirmed by the variation of peak-to-peak separation (ΔE_P) in the CV curves of different rhGO electrodes (Table 1). The rhGO electrodes with a higher area percentage of nanoholes tend to have smaller ΔE_P, meaning that a lower driving potential is required to trigger the redox reactions.[54] Thus, the high area percentage of nanoholes are beneficial to the faster heterogeneous electron transfer. Secondly, the nanoholes on rhGO provide abundant shortcuts for ion transportation, leading to faster diffusion kinetics. When ions participate in redox reactions, a diffusion layer gradually forms, where redox reactants are depleted, and further redox reactions are controlled by the ion diffusion rate.[54] In rhGO, ions transport via nanoholes and thus can deliver charges on the rhGO sheets located deeper from the electrode surface, causing a part of the diffusion layer overlapped by the depth of the rhGO electrode. Therefore, compared to the rGO counterpart, the diffusion layer above the surface of the rhGO electrode should be thinner, which facilitates the ion diffusion. The ion diffusion coefficient can be given by the Randles-Sevcik equation[9, 51-52, 54]

$$i_p = 0.4463\, n^{\frac{3}{2}} F^{\frac{3}{2}} A c (v D_{\mathrm{R-S}}/RT)^{1/2} \tag{3}$$

where i_p is the peak current (A), n is the number of electron transfer (here is 1), c is the concentration of $[\mathrm{Fe(CN)_6}]^{3-}$ ions (mol/ml), v is the scan rate (V/s), and $D_{\mathrm{R\text{-}S}}$ represents the diffusion coefficient (cm^2/s) of $[\mathrm{Fe(CN)_6}]^{3-}$ ions calculated from the Randles-Sevcik equation. By plotting i_P versus $v^{1/2}$ (i.e. the Randles-Sevcik plot), the ion diffusion coefficient can be calculated from eq 3 using the slope of the curve. As shown in Figures 6c and S11, good linear correlations between i_P and $v^{1/2}$ are observed in all samples. The calculation results (Table 1) based on eq 3 show that the ion diffusion coefficients in rhGO are at least three orders of magnitude higher than that in rGO (2.12×10^{-9} cm^2/s). The rhGO-PL electrode has the highest ion diffusion coefficients of 9.94×10^{-6} cm^2/s. The ion diffusion rate increases with the area percentage of nanoholes on rhGO, except for rhGO-EL that shows a slight drop compared with rhGO-EM.

The EIS Nyquist plot shown in Figure 6d further demonstrates the distinct redox kinetics and diffusion kinetics between rhGO and rGO, as indicated by different behaviors in both high- and low-frequency ranges. As shown in Table 1, the values of R_CT in rhGO are all at least 20 Ω smaller than that in rGO, confirming the faster heterogeneous electron transfer on rhGO relative to rGO. Among the rhGO electrodes, the heterogeneous electron transfer becomes faster with increasing area percentage of nanoholes, and the only exception is rhGO-EL that shows a slight drop. This is consistent with the trend of $D_{\mathrm{R\text{-}S}}$. In addition, the diffusion kinetics can be quantified with the EIS data using the Warburg plot. As shown in Figure 6e, rhGO-PL shows a much lower slope in the

Warburg plot compared to rGO, suggesting a smaller Warburg coefficient. The calculation results (Table 1) of ion diffusion coefficients based on eqs 1 and 2 agree well with those obtained based on eq 3. These results confirm again that the high area percentage of nanoholes can improve the catalytic activity by providing more electrochemically active sites.

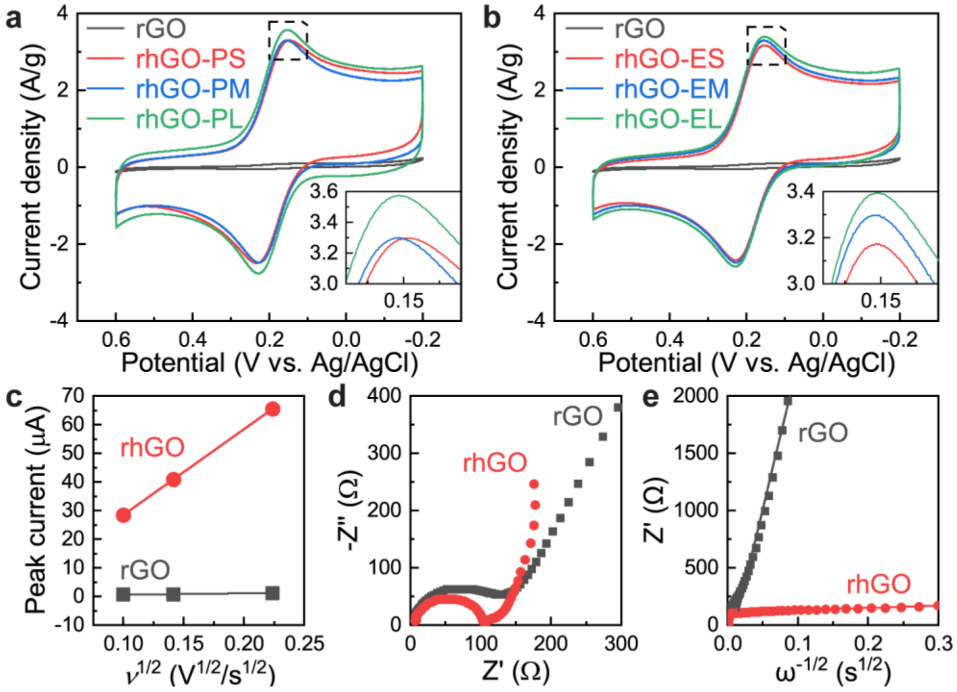

Figure 6. Electrochemical catalytic activity of reduced holey graphene oxide (rhGO) in 5 mM $K_3[Fe(CN)_6]$ and 0.1 M KCl: (a,b) CV curves at a scan rate of 10 mV/s; (c) Randles-Sevcik plot measured at scan rates of 10–50 mV/s; (d) Nyquist plot; (e) Warburg plot. Insets in a,b respectively magnify the positive redox peaks indicated by the dash lines.

CONCLUSIONS

The fabrication of holey graphene with excellent capacitive performance and electrochemical catalytic activity was achieved within a few minutes via the MACE method, which was much faster than conventional hour-scale approaches. Moreover, the population, average diameter, area percentage of nanoholes on holey graphene sheets were effectively controlled by a two-step strategy combining pretreatment and MACE to further promote the electrochemical properties. This microwave-assisted method was fast, controllable, totally solution-based, and thus favorable to be employed in large-scale manufacturing for various applications.

The structural characterizations provided insights into the nucleation and growth of nanoholes during each step of fabrication. The pretreatment caused a partial reduction of GO sheets with an increased defect density. The MACE resulted in the fast growth of nanoholes due to the coupling effect of microwave irradiation and hydrogen peroxide chemical etching. We also elucidated the mechanism of the rapid fabrication process. During the MACE, the microwave-induced selective heating of GO sheets by both localized Joule heating and dielectric heating, which facilitated the effective etching of GO sheets and limited the decomposition of hydrogen peroxide during processing. In electrochemical measurements, the nanoholes on holey graphene significantly improved the accessible surface area of the electrode, heterogeneous electron transfer, and ion diffusion kinetics, demonstrating the great application potential of the microwave-fabricated holey graphene in the fields of energy storage and electrochemical catalysis.

EXPERIMENTAL PROCEDURES

Pretreatment of Graphene Oxide. The GO aqueous solution was first prepared by the improved Hummer's method.[56] For the microwave pretreatment, a 3 mg/mL GO aqueous solution was added into a glass reaction tube sealed by a PTFE cap and heated in a microwave reactor (Anton Paar Monowave 400, 2.45 GHz) at a constant power of 50 W for 90–360 s with magnetic stirring at a speed of 600 rpm. The temperature profile per second was recorded by an infrared thermometer. Meanwhile, a pressure sensor collected the variation of pressure inside the reaction tube. Compressed air flow was used to cool down the solution to room temperature after heating.

Holey Graphene Fabrication. The pretreated GO solution and hydrogen peroxide aqueous solution (30%) were mixed in a reaction tube with a volume ratio of 5:2. The mixture was heated in the microwave reactor with a constant power of 50 W for 45–180 s. After cooling, the solution was centrifuged at 30k rpm for 15 min to remove residual hydrogen peroxide. The precipitate was then re-dispersed in de-ionized water to form the hGO aqueous solution. To obtain rhGO, the hGO aqueous solution was heated in the microwave reactor to 220 °C and held for 90 s.

Microstructural Characterization. The morphologies of graphene sheets were characterized on an aberration-corrected TEM (FEI Titan 300/80) using the electron beam with an acceleration voltage of 300 kV. AFM was performed on a Bruker Multimode 8 system using the contact mode. Chemical compositions of graphene samples were analyzed on an XPS system (VG Escalab 220i-XL) with a monochromatic Al K-alpha source. Raman spectra were collected using a 532-nm laser. Each spectrum was scanned 10 times with 1-s duration per scan. The spectrum center and filter grating were 2050 cm^{-1} and 600 g/mm, respectively.

Electrochemical Measurements. All electrochemical measurements were carried out on a CH Instruments 660E workstation at ambient condition using a three-electrode setup that included a 0.5 mm Pt wire (CH Instruments) as the counter electrode, a Ag/AgCl reference electrode in 1 M KCl (+0.235 V vs. standard hydrogen electrode), and a glassy carbon working electrode (GCE). For each measurement, the working electrode was prepared by drop-casting 10 μg active material on a freshly polished GCE (polished with 0.05 μm alumina powder and rinsed by de-ionized water). For the measurements in 1 M Na_2SO_4 aqueous electrolyte, the CV curves were measured with a potential window from −0.2 to 0.8 V vs. Ag/AgCl. The internal-resistance drop was compensated at each scan. The GCD curves were obtained from −0.2 to 0.8 V vs. Ag/AgCl. EIS measurements were performed at the open-circuit voltage from 1 MHz to 1 Hz at a bias voltage of

5 mV. For the measurements in 5 mM $K_3[Fe(CN)_6]$ and 0.1 M KCl aqueous electrolyte, the CV curves were measured with a potential window from −0.2 to 0.6 V vs. Ag/AgCl. EIS measurements were performed at the same condition as above.

ASSOCIATED CONTENT

Supporting Information.

Supplemental details for experimental procedures, supporting figures and tables.

AUTHOR INFORMATION

Corresponding Author

*Email: qiong.nian@asu.edu.

Author Contributions

The manuscript was written through the contributions of all authors. All authors approved the final version.

Notes

The authors declare no conflicts of interests with the contents of this article.

ACKNOWLEDGMENT

This study is partially supported by ASU startup funds, NSF grant CMMI-1825576. We acknowledge the use of facilities within the Eyring Materials Center at Arizona State University supported in part by NNCI-ECCS-1542160. We also appreciate the assistance of Dr. Q. H. Wang and her group members in Raman spectroscopy study.

REFERENCES

1. Novoselov, K. S.; Fal'ko, V. I.; Colombo, L.; Gellert, P. R.; Schwab, M. G.; Kim, K., A roadmap for graphene. *Nature* **2012,** *490* (7419), 192-200.

2. Wang, T.; Huang, D.; Yang, Z.; Xu, S.; He, G.; Li, X.; Hu, N.; Yin, G.; He, D.; Zhang, L., A Review on Graphene-Based Gas/Vapor Sensors with Unique Properties and Potential Applications. *Nanomicro Lett* **2016,** *8* (2), 95-119.

3. Wang, H.; Maiyalagan, T.; Wang, X., Review on Recent Progress in Nitrogen-Doped Graphene: Synthesis, Characterization, and Its Potential Applications. *ACS Catalysis* **2012,** *2* (5), 781-794.

4. Han, X.; Yang, Z.; Zhao, B.; Zhu, S.; Zhou, L.; Dai, J.; Kim, J.-W.; Liu, B.; Connell, J. W.; Li, T.; Yang, B.; Lin, Y.; Hu, L., Compressible, Dense, Three-Dimensional Holey Graphene Monolithic Architecture. *ACS Nano* **2017,** *11* (3), 3189-3197.

5. Xu, Y.; Lin, Z.; Zhong, X.; Huang, X.; Weiss, N. O.; Huang, Y.; Duan, X., Holey graphene frameworks for highly efficient capacitive energy storage. *Nat Commun* **2014,** *5*, 4554.

6. Raccichini, R.; Varzi, A.; Passerini, S.; Scrosati, B., The role of graphene for electrochemical energy storage. *Nature Materials* **2014,** *14*, 271.

7. Sun, Y.; Wu, Q.; Shi, G., Graphene based new energy materials. *Energy & Environmental Science* **2011,** *4* (4), 1113-1132.

8. Pumera, M., Graphene-based nanomaterials and their electrochemistry. *Chem Soc Rev* **2010,** *39* (11), 4146-57.

9. Yuan, W.; Zhou, Y.; Li, Y.; Li, C.; Peng, H.; Zhang, J.; Liu, Z.; Dai, L.; Shi, G., The edge- and basal-plane-specific electrochemistry of a single-layer graphene sheet. *Scientific Reports* **2013,** *3*, 2248.

10. Sun, H.; Mei, L.; Liang, J.; Zhao, Z.; Lee, C.; Fei, H.; Ding, M.; Lau, J.; Li, M.; Wang, C.; Xu, X.; Hao, G.; Papandrea, B.; Shakir, I.; Dunn, B.; Huang, Y.; Duan, X., Three-dimensional holey-graphene/niobia composite architectures for ultrahigh-rate energy storage. *Science* **2017,** *356* (6338), 599-604.

11. Alsharaeh, E.; Ahmed, F.; Aldawsari, Y.; Khasawneh, M.; Abuhimd, H.; Alshahrani, M., Novel synthesis of holey reduced graphene oxide (HRGO) by microwave irradiation method for anode in lithium-ion batteries. *Scientific Reports* **2016,** *6*, 29854.

12. Zhao, X.; Hayner, C. M.; Kung, M. C.; Kung, H. H., Flexible holey graphene paper electrodes with enhanced rate capability for energy storage applications. *ACS nano* **2011,** *5* (11), 8739-8749.

13. Walsh, E. D.; Han, X.; Lacey, S. D.; Kim, J.-W.; Connell, J. W.; Hu, L.; Lin, Y., Dry-Processed, Binder-Free Holey Graphene Electrodes for Supercapacitors with Ultrahigh Areal Loadings. *ACS Applied Materials & Interfaces* **2016,** *8* (43), 29478-29485.

14. Han, X.; Funk, M. R.; Shen, F.; Chen, Y.-C.; Li, Y.; Campbell, C. J.; Dai, J.; Yang, X.; Kim, J.-W.; Liao, Y.; Connell, J. W.; Barone, V.; Chen, Z.; Lin, Y.; Hu, L., Scalable Holey Graphene Synthesis and Dense Electrode Fabrication toward High-Performance Ultracapacitors. *ACS Nano* **2014,** *8* (8), 8255-8265.

15. Zhai, S.; Wang, C.; Karahan, H. E.; Wang, Y.; Chen, X.; Sui, X.; Huang, Q.; Liao, X.; Wang, X.; Chen, Y., Nano-RuO2-Decorated Holey Graphene Composite Fibers for Micro-Supercapacitors with Ultrahigh Energy Density. *Small* **2018,** *14* (29), 1800582.

16. Zhao, J.; Zhang, Y.-Z.; Zhang, F.; Liang, H.; Ming, F.; Alshareef, H. N.; Gao, Z., Partially Reduced Holey Graphene Oxide as High Performance Anode for Sodium-Ion Batteries. *Advanced Energy Materials* **2019,** *9* (7), 1803215.

17. Zhu, C.; Hui, Z.; Pan, H.; Zhu, S.; Zhang, Q.; Mao, J.; Guo, Z.; Li, Y.; Imtiaz, M.; Chen, Z., Ultrafast Li-ion migration in holey-graphene-based composites constructed by a generalized ex situ method towards high capacity energy storage. *Journal of Materials Chemistry A* **2019,** *7* (9), 4788-4796.

18. Zheng, Q.; Geng, Y.; Wang, S.; Li, Z.; Kim, J.-K., Effects of functional groups on the mechanical and wrinkling properties of graphene sheets. *Carbon* **2010,** *48* (15), 4315-4322.

19. Han, T. H.; Huang, Y.-K.; Tan, A. T.; Dravid, V. P.; Huang, J., Steam etched porous graphene oxide network for chemical sensing. *J. Am. Chem. Soc.* **2011,** *133* (39), 15264-15267.

20. Wang, X.; Jiao, L.; Sheng, K.; Li, C.; Dai, L.; Shi, G., Solution-processable graphene nanomeshes with controlled pore structures. *Sci. Rep.* **2013,** *3*.

21. Zhu, Y.; Murali, S.; Stoller, M. D.; Ganesh, K.; Cai, W.; Ferreira, P. J.; Pirkle, A.; Wallace, R. M.; Cychosz, K. A.; Thommes, M., Carbon-based supercapacitors produced by activation of graphene. *Science* **2011,** *332* (6037), 1537-1541.

22. Lin, Y.; Watson, K. A.; Kim, J.-W.; Baggett, D. W.; Working, D. C.; Connell, J. W., Bulk preparation of holey graphene via controlled catalytic oxidation. *Nanoscale* **2013,** *5* (17), 7814-7824.

23. Zhao, Y.; Hu, C.; Song, L.; Wang, L.; Shi, G.; Dai, L.; Qu, L., Functional graphene nanomesh foam. *Energy Environ. Sci.* **2014,** *7* (6), 1913-1918.

24. Radich, J. G.; Kamat, P. V., Making graphene holey. Gold-nanoparticle-mediated hydroxyl radical attack on reduced graphene oxide. *ACS nano* **2013,** *7* (6), 5546-5557.

25. Xu, Y.; Chen, C.-Y.; Zhao, Z.; Lin, Z.; Lee, C.; Xu, X.; Wang, C.; Huang, Y.; Shakir, M. I.; Duan, X., Solution Processable Holey Graphene Oxide and Its Derived Macrostructures for High-Performance Supercapacitors. *Nano Letters* **2015,** *15* (7), 4605-4610.

26. Kotal, M.; Kim, H.; Roy, S.; Oh, I., Sulfur and Nitrogen Co-Doped Holey Graphene Aerogel for Structurally Resilient Solid-State Supercapacitors under High-Compressions. *Journal of Materials Chemistry A* **2017**.

27. Liu, J.; Du, P.; Wang, Q.; Liu, D.; Liu, P., Mild synthesis of holey N-doped reduced graphene oxide and its double-edged effects in polyaniline hybrids for supercapacitor application. *Electrochimica Acta* **2019,** *305*, 175-186.

28. Wang, C.; Zhai, S.; Yuan, Z.; Chen, J.; Zhang, X.; Huang, Q.; Wang, Y.; Liao, X.; Wei, L.; Chen, Y., A core-sheath holey graphene/graphite composite fiber intercalated with MoS2 nanosheets for high-performance fiber supercapacitors. *Electrochimica Acta* **2019**.

29. Lacey, S. D.; Walsh, E. D.; Hitz, E.; Dai, J.; Connell, J. W.; Hu, L.; Lin, Y., Highly compressible, binderless and ultrathick holey graphene-based electrode architectures. *Nano Energy* **2017,** *31*, 386-392.

30. Kirsch, D. J.; Lacey, S. D.; Kuang, Y.; Pastel, G.; Xie, H.; Connell, J. W.; Lin, Y.; Hu, L., Scalable Dry Processing of Binder-Free Lithium-Ion Battery Electrodes Enabled by Holey Graphene. *ACS Applied Energy Materials* **2019**.

31. Peng, Y.-Y.; Liu, Y.-M.; Chang, J.-K.; Wu, C.-H.; Ger, M.-D.; Pu, N.-W.; Chang, C.-L., A facile approach to produce holey graphene and its application in supercapacitors. *Carbon* **2015,** *81*, 347-356.

32. Patel, M.; Feng, W.; Savaram, K.; Khoshi, M. R.; Huang, R.; Sun, J.; Rabie, E.; Flach, C.; Mendelsohn, R.; Garfunkel, E.; He, H., Microwave Enabled One-Pot, One-Step Fabrication and Nitrogen Doping of Holey Graphene Oxide for Catalytic Applications. *Small* **2015,** *11* (27), 3358-3368.

33. Savaram, K.; Li, M.; Tajima, K.; Takai, K.; Hayashi, T.; Hall, G.; Garfunkel, E.; Osipov, V.; He, H., Dry microwave heating enables scalable fabrication of pristine holey graphene nanoplatelets and their catalysis in reductive hydrogen atom transfer reactions. *Carbon* **2018,** *139*, 861-871.

34. Lin, L.; Peng, H.; Liu, Z., Synthesis challenges for graphene industry. *Nature Materials* **2019,** *18* (6), 520-524.

35. Bagri, A.; Mattevi, C.; Acik, M.; Chabal, Y. J.; Chhowalla, M.; Shenoy, V. B., Structural evolution during the reduction of chemically derived graphene oxide. *Nature Chemistry* **2010,** *2*, 581.

36. Kumatani, A.; Miura, C.; Kuramochi, H.; Ohto, T.; Wakisaka, M.; Nagata, Y.; Ida, H.; Takahashi, Y.; Hu, K.; Jeong, S.; Fujita, J.-i.; Matsue, T.; Ito, Y., Chemical Dopants on Edge of Holey Graphene Accelerate Electrochemical Hydrogen Evolution Reaction. *Advanced Science* **2019,** *6* (10), 1900119.

37. Banerjee, S.; Shim, J.; Rivera, J.; Jin, X.; Estrada, D.; Solovyeva, V.; You, X.; Pak, J.; Pop, E.; Aluru, N.; Bashir, R., Electrochemistry at the Edge of a Single Graphene Layer in a Nanopore. *ACS Nano* **2013,** *7* (1), 834-843.

38. Zhu, Y.; Murali, S.; Stoller, M. D.; Velamakanni, A.; Piner, R. D.; Ruoff, R. S., Microwave assisted exfoliation and reduction of graphite oxide for ultracapacitors. *Carbon* **2010,** *48* (7), 2118-2122.

39. Chen, W. F.; Yan, L. F.; Bangal, P. R., Preparation of graphene by the rapid and mild thermal reduction of graphene oxide induced by microwaves. *Carbon* **2010,** *48* (4), 1146-1152.

40. Kudin, K. N.; Ozbas, B.; Schniepp, H. C.; Prud'homme, R. K.; Aksay, I. A.; Car, R., Raman Spectra of Graphite Oxide and Functionalized Graphene Sheets. *Nano Letters* **2008,** *8* (1), 36-41.

41. Ferrari, A. C.; Basko, D. M., Raman spectroscopy as a versatile tool for studying the properties of graphene. *Nat Nano* **2013,** *8* (4), 235-246.

42. Dresselhaus, M. S.; Jorio, A.; Hofmann, M.; Dresselhaus, G.; Saito, R., Perspectives on Carbon Nanotubes and Graphene Raman Spectroscopy. *Nano Letters* **2010,** *10* (3), 751-758.

43. Cançado, L. G.; Jorio, A.; Ferreira, E. H. M.; Stavale, F.; Achete, C. A.; Capaz, R. B.; Moutinho, M. V. O.; Lombardo, A.; Kulmala, T. S.; Ferrari, A. C., Quantifying Defects in Graphene via Raman Spectroscopy at Different Excitation Energies. *Nano Letters* **2011,** *11* (8), 3190-3196.

44. Jiang, W.-S.; Yang, C.; Chen, G.-X.; Yan, X.-Q.; Chen, S.-N.; Su, B.-W.; Liu, Z.-B.; Tian, J.-G., Preparation of high-quality graphene using triggered microwave reduction under an air atmosphere. *Journal of Materials Chemistry C* **2018,** *6* (7), 1829-1835.

45. Hu, H.; Zhao, Z.; Zhou, Q.; Gogotsi, Y.; Qiu, J., The role of microwave absorption on formation of graphene from graphite oxide. *Carbon* **2012,** *50* (9), 3267-3273.

46. Kang, S.; Choi, H.; Lee, S. B.; Park, S. C.; Park, J. B.; Lee, S.; Kim, Y.; Hong, B. H., Efficient heat generation in large-area graphene films by electromagnetic wave absorption. *2D Materials* **2017,** *4* (2), 025037.

47. Voiry, D.; Yang, J.; Kupferberg, J.; Fullon, R.; Lee, C.; Jeong, H. Y.; Shin, H. S.; Chhowalla, M., High-quality graphene via microwave reduction of solution-exfoliated graphene oxide. *Science* **2016,** *353* (6306), 1413-1416.

48. Wang, C.; Han, X.; Xu, P.; Zhang, X.; Du, Y.; Hu, S.; Wang, J.; Wang, X., The electromagnetic property of chemically reduced graphene oxide and its application as microwave absorbing material. *Applied Physics Letters* **2011,** *98* (7), 072906.

49. Zhu, Y.; Stoller, M. D.; Cai, W.; Velamakanni, A.; Piner, R. D.; Chen, D.; Ruoff, R. S., Exfoliation of Graphite Oxide in Propylene Carbonate and Thermal Reduction of the Resulting Graphene Oxide Platelets. *ACS Nano* **2010,** *4* (2), 1227-1233.

50. Bonaccorso, F.; Colombo, L.; Yu, G.; Stoller, M.; Tozzini, V.; Ferrari, A. C.; Ruoff, R. S.; Pellegrini, V., Graphene, related two-dimensional crystals, and hybrid systems for energy conversion and storage. *Science* **2015,** *347* (6217), 1246501.

51. Bard, A. J.; Faulner, L. R., *Electrochemical methods: fundamentals and applications*. 2rd ed.; Wiley: New York, 2001; p 718.

52. Zanello, P., *Inorganic Electrochemistry: Theory, Practice and Application*. The Royal Society of Chemistry: Cambridge, UK, 2003.

53. Randles, J. E. B., Kinetics of rapid electrode reactions. *Discussions of the Faraday Society* **1947,** *1* (0), 11-19.

54. Elgrishi, N.; Rountree, K. J.; McCarthy, B. D.; Rountree, E. S.; Eisenhart, T. T.; Dempsey, J. L., A Practical Beginner's Guide to Cyclic Voltammetry. *Journal of Chemical Education* **2018,** *95* (2), 197-206.

55. Shang, N. G.; Papakonstantinou, P.; McMullan, M.; Chu, M.; Stamboulis, A.; Potenza, A.; Dhesi, S. S.; Marchetto, H., Catalyst ‐ Free Efficient Growth, Orientation and Biosensing Properties of Multilayer Graphene Nanoflake Films with Sharp Edge Planes. *Advanced Functional Materials* **2008,** *18* (21), 3506-3514.

56. Marcano, D. C.; Kosynkin, D. V.; Berlin, J. M.; Sinitskii, A.; Sun, Z.; Slesarev, A.; Alemany, L. B.; Lu, W.; Tour, J. M., Improved Synthesis of Graphene Oxide. *ACS Nano* **2010,** *4* (8), 4806-4814.